Effect of deposition time on properties of the ZnO by USD Method

N. Madaoui[a], M. Azibi[a], I. Djabrouhou[b], and N. Saoula[a]

[a]*Centre de Développement des Technologies Avancées Cité du 20 Août 1956, Baba Hassan, Alger, Algérie*

[b]*Laboratory of Energy and Smart Systems, Faculty of Science and Technology, University of Khemis Miliana, Road of Theniyet Elhad, Khemis Miliana 44225, Ain Defla, Algeria.*

Received 10 September 2023; accepted 5 November 2023

This investigation aims to improve the properties of 304 L stainless steel (SS) substrates for use in corrosion, mechanical, and biomedical applications by depositing ZnO thin films. The ultrasonic spraying technique was used to prepare ZnO thin films with depositional times of 1, 4, and 9 minutes. XRD and Raman studied the surface characteristics of ZnO samples. XRD analysis revealed a hexagonal structure with an average crystallite size of 22 nm for ZnO. Indentation nano measurements indicated an increase in the hardness of the films examined. To determine the type of conductivity and estimate the charge carrier density, potentiodynamic polarization, electrochemical impedance spectroscopy (EIS), and Mott-Schottky analysis were performed. The thin film deposited for 9 minutes was found to be the most effective in improving corrosion resistance.

Keywords: 304 L Stainless steel (SS); ZnO thin films; ultrasonic spray deposition (USD) technique; and corrosion behavior.

DOI: https://doi.org/10.31349/RevMexFis.70.031001

1. Introduction

Stainless Steel (SS), such as 304 L, is a widely used material in both industrial and biomedical applications [1] (orthodontics and implants such as brackets, and screws) due to its good mechanical properties and high resistance to corrosion [2-4]. However, it is susceptible to localized corrosion in the presence of chloride ions or other aggressive species, and the release of toxic metallic ions can have undesirable effects on bone tissues. Solvated metals are not biodegradable in the human body [5]. Thin films are frequently used to protect metals and alloys from the attack of corrosive species. In recent decades, the field of thin film technology has emerged worldwide as an influential area of research owing to its potential applications in several devices.

Thin films have been widely used to protect metals and alloys against corrosive attack. In recent years, the development of thin film technology has become an influential area of research due to its potential applications in various devices.

Nano-sized transition metal-based oxides (like ZnO, SiO_2, TiO_2, CuO, etc) have attracted significant interest due to their capacity to enhance the chemical, physical and electrical properties [6]. Zinc is considered very abundant in bone tissue. It is involved in many physiological functions of the immune system and is an essential element in cell growth [5]. Zinc exhibits good efficacy against gram-positive bacteria. It reduces the adhesion of bacteria and inhibits the growth of S. aureus bacteria [7]. The best thin films for cell adhesion and development are those that contain zinc in their composition compared to films without zinc [8]. ZnO is inexpensive, handy, nontoxic, biocompatible [9], biodegradable [10], non-volatile, and the most biosafe semiconductor material [9]. It is widely used for numerous applications such as gas sensors [11], biosensors [12], drugs, cosmetics, storage, optical and electrical devices, solar cells [13], and biomedical applications [14-17]. To deposit ZnO thin film, several methods have been often used such as chemical vapor deposition [18,19], pulsed laser deposition [10,20], atomic layer deposition (ALD) [21,22], spray pyrolysis [13], RF magnetron sputtering [23,24], plasma spraying [25], dip-coating method [26], electron beam (e-beam) evaporation [27], chemical bath deposition [28], chemical oxidative polymerization [29], plasma electrolytic oxidation (PEO) [30], electrophoretic deposition (EPD) [31], and sol-gel [32], etc. Among these methods, we are going to focus on the spray ultrasonic technique [33] because of its simplicity and suitability for large-scale production. There are multiple benefits associated with the production of nanocrystalline thin films, such as the relatively thin and homogeneous composition of its structure, and easy control of the film thickness. This method is less hazardous due to the closed system used in this process. It is possible to modify the electrical, mechanical, magnetic, and optical properties of ZnO nanostructures [34]. In this paper, different ZnO thin film deposition times were prepared on a 304 L stainless steel surface by ultrasonic sputtering. As far as we are aware, this is the initial occasion on which the process of applying a ZnO coating onto 304L alloy through ultrasonic spray deposition has been utilized to produce a film with exceptional mechanical strength and resistance against corrosion. XRD and Raman investigated the thin films' crystalline and chemical structure. Nanoindentation was used to examine mechanical properties at the nanoscale. In electrochemical studies, potentiodynamic polarization measurement, electrochemical impedance spectroscopy (EIS), and the Mot-Schottky method (MS) were performed to evaluate the corrosion behaviours of 304L SS immersed in Ringer media with and without ZnO thin films.

TABLE I. Chemical composition of 304L SS (wt%).

Elements (wt%)	C	Mn	Si	P	S	Cr	Ni	Mo	Al	Cu	Co	V	Nb	Ti	Sn	W
AISI 304L	0.023	1.287	0.402	0.040	0.002	18.044	8.009	0.183	0.004	0.279	0.186	0.059	0.012	0.002	0.009	0.028

Nb	Ti	Sn	W	Co	V
0.012	0.002	0.009	0.028	0.186	0.059

2. Materials and methods

2.1. Substrate preparation

The chemical composition in weight percentage ($wt.\%$) of the commercially stainless steels [35] is given in Table I. Substrates with dimensions of $\phi = 10$ mm and a thickness of 4 mm was used as the substrate. The substrate work surfaces were polished sequentially with silicon carbide papers of 400, 600, 800, 1000, and 4000 grit. The substrates were then mechanically polished using an alumina solution in a MECAPOL P230 polisher until a mirror-like finish was achieved. The average surface roughness (Ra) of the polished substrates was measured to be 90 nm. Before the deposition of ZnO, the substrates were subjected to a cleaning procedure that involved sonication in acetone for 2 minutes, followed by sonication in ethanol for 5 minutes. The substrates were then cleaned in deionized water for 2 minutes and dried with compressed air.

2.2. Deposition of ZnO

ZnO thin films were deposited on a 304L substrate by using the ultrasonic spraying method. We used zinc acetate ($C_4H_6O_4Zn.2H_2O$) as the source material of ZnO which we dissolved in methanol as the solvent. The concentration of the solution was set to 0.1 moles/L. Table II shows the deposition conditions. After removing the solvent, the next step is to proceed with thermal densification to eliminate any residual organic species. This is accomplished through a thermal annealing process conducted in a TR 28-3T oven. The oven is carefully heated at a rate of 10°C per minute until it reaches the designated annealing temperature, $T = 600$°C.

2.3. Instruments and methods

The structural properties of the films were assessed using Xray diffraction (XRD) analysis. A Bruker Axe D8 Advance diffractometer, operating in the Bragg-Brentano geometry with CuKα radiation (λ)= 1.5406 Å and a power of 2200 Watts was employed. XRD measurements were performed in a (θ) /(2θ) configuration with a diffraction angle ranging from 20° to 80°. The step size for data acquisition was set at 0.02° with a sampling interval of 4 seconds.

Raman spectra were acquired using a HORIBA Jobin Yvon T64000 micro-Raman spectrometer. The spectral range investigated was (100-800) cm^{-1}. Excitation is using a 633 nm laser line delivering 10 mW of power during the measurement. The nanoindentation [36] was employed to evaluate the mechanical characteristics. of ZnO films. Using a nanoindenter with a Berkovich tip, the CSM Instrument Switzerland performed measurements of Young's modulus Y and hardness H on nanostructured surfaces. This approach provides valuable data to evaluate the mechanical behavior of the films and to improve their suitability for specific applications. The interaction between the indenter and the film surface was sim-

TABLE II. Conditions for preparing the ZnO thin films.

Coating	ZnO
Basic precursors	acetate de zinc ($C_4H_6O_4Z_n$, $2H_2O$)
Solvent	methanol
The concentration of the solution (mol/l)	0.1
Carrier gas	Nitrogen (N_2)
Substrates	Silicon and Stainless steel (304 L)
Substrate temperature (°C)	480
Spray frequency (kHz)	40
Spray rate (ml/min)	8
Deposition time (min)	1, 4 and 9
Distance nozzle-substrate (cm)	10

simulated as frictionless in nanoindentation. To avoid the effect of the substrate, the maximum indentation depth in all tests is not greater than 10% of the film thickness [37]. For each load, Average values of Young's modulus Y and hardness H were acquired by making several indentations at various points on the film surface. The indentation depth h, Young's modulus Y, and hardness H of the thin films as a function of applied load were determined from the load-displacement curves. We operated the indenter in the continuous stiffness mode with a maximum load of 1 mN. The applied load is 1 mN with a loading and unloading rate of 2 mN/min, a Poisson's coefficient of 0.26, a spacing of 10 s, and an acquisition rate of 10 Hz. The hardness H and Young's modulus Y of the thin films are quantitatively calculated based on the Oliver-Pharr method [38].

To investigate the electrochemical properties of the films, various tests were conducted, including open circuit potential (OCP), potentiodynamic polarization measurement, electrochemical impedance spectroscopy (EIS), and Mott-Schottky (MS) tests. To perform the analysis, a conventional three-electrode cell was employed and connected to a potentiostat/galvanostat (PARSTAT 4000, Princeton Applied Research, USA). Before initiating the electrochemical testing, the working electrode, wrapped in a Teflon sample holder with a 0.5 cm exposed area, was immersed in the solution for 12 hours to stabilize the open-circuit voltage (OCP). The potential across the electrochemical interface was measured using a reference electrode (SCE), while the corrosion current densities (icorr) across the interface were measured using a graphite counter electrode ($\phi = 0.5$ mm). Corrosion resistance in physiological environments is an important consideration when selecting materials for implants. Therefore, the electrolyte used in this study was a body-simulated fluid based on Ringer's physiological formulation, comprising 8.5 g/dm^3 Sodium chloride (NaCl), 0.25 g/dm^3 Potassium Chloride (KCl), 0.22 g/dm^3 Calcium Chloride ($CaCl_2$), and 0.15 g/dm^3 Sodium Bicarbonate ($NaHCO_3$). Potentiodynamic curves (Tafel curves) were measured after 12 hours of immersion, ranging between ± 250 mV (vs. SCE), with a scanning speed of 1 mV/s. The VersaStudio software was used to acquire and analyze the data.

All tests were performed at a body temperature of 37°C, maintaining a precise thermostatic bath with a precision of 2°C during each experiment. In the Ringer physiological solution, Nyquist plot tests were performed with a frequency range of 0.01 to 100 kHz and a sinusoidal tension of 10 mV. The Mott-Schottky evaluation was carried out using a 1 kHz frequency, with a potential range varied from 0.2 to 2.2 Volt in the Ringer solution. The EIS and M-S data were processed using Zview software.

3. Results and discussions

The X-ray diffraction patterns of various disposition times of ZnO films are illustrated in Fig. 1.

All diffraction spectra reveal the typical wurtzite-type structured ZnO [39]. All samples display the characteristic wurst-type structure of ZnO in their diffraction spectra. (JCPDS No.75-1526). However, when the deposition times were increased to 9 min, some impurity peaks with lower intensities appeared at diffraction 2(θ) angles of 40.9, 43, and 50.8° (marked with an asterisk in Fig. 1), which can be attributed to zinc carbonate hydroxide hydrate (JCPDS No. 11-0287). It should be noted that the crystallization of the film improved as the deposition time increased. The ZnO films exhibited a preferred orientation in the (002) direction. The mechanism behind the orientation evolution in the films has been explained by the interplay between surface energy and strain energy. The ZnO film tends to grow towards the (002) direction, the fact that it has the lowest surface free energy [40]. The average grain sizes D of the films were estimated by the Williamson-Hall method [41] using the following Eq. (1):

$$\beta \cos\theta = \frac{K\,\lambda}{D} + \epsilon \sin\theta, \tag{1}$$

where k is the constant depending on the crystallite shape, lambda (nm) represents the wavelength of (CuKα) radiation (1.5418 Å) θ (rad) is the Bragg angle of the X-ray diffraction peak, β is the stands full width at half-maximum (FWHM) value of the diffraction peak and ϵ is the lattice strain. The dislocation line length per unit volume of crystal is characterized as the dislocation density δ, which describes the number of defects in the coating [42]. The following Eqs. (2) (3) and (4) are used to calculate the dislocation density and the lattice constants of the a and c axis of the ZnO thin films [43-45].

$$\sigma = \frac{1}{D^2}, \tag{2}$$

$$2d \sin\theta = n\lambda, \tag{3}$$

$$\frac{1}{D^2} = \left(\frac{4[h^2 + hk + l^2]}{3a^2} + \frac{l^2}{c^2}\right). \tag{4}$$

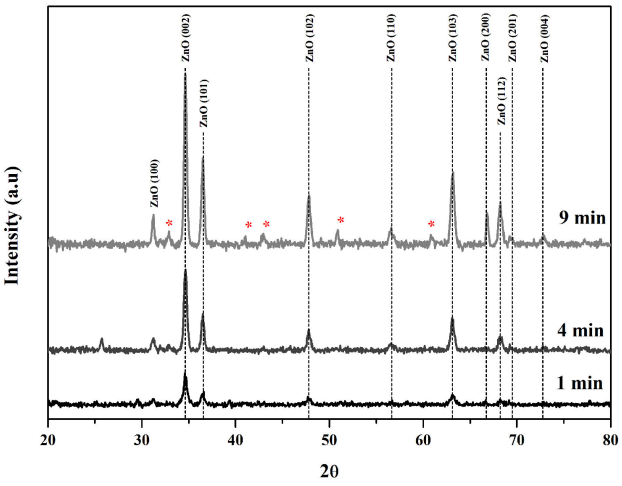

FIGURE 1. XRD patterns with different deposition times (1, 4, and 9 min) of ZnO thin films.

TABLE III. Structural properties of ZnO thin films (wurtzite).

Substrates	Silicon (100)											
deposition time (min)	1				4				9			
hkl (nm)	002	101	102	103	002	101	102	103	002	101	102	103
$2\theta^\circ$	34.7	36.5	47.8	63.1	34.7	36.5	47.8	63.1	34.7	36.5	47.8	63.1
FWHM $(\beta)^\circ$	0.48	0.45	0.5	0.57	0.39	0.37	0.43	0.47	0.35	0.36	0.40	0.45
d_{hkl} (nm)	25.8	24.6	19.0	14.7	25.8	24.6	19.0	14.7	25.8	24.6	19.0	14.7
Texture coefficient (TC)	0.52	0.20	0.11	0.16	0.51	0.20	0.11	0.18	0.44	0.21	0.12	0.22
Average lattice strain, $\varepsilon(10^{-3})$	3.5				3.1				3.8			
Cristallite size, D (nm)	22				27				30			
Dislocation density $\delta(10^{-3}\text{nm}^{-3})$	2.1				1.3				1.1			
Lattice constant a (A°)	3.24											
Lattice constant c (A°)	5.19											

Table III gives the information on structural properties of samples, including FWHM, the average crystallite size D, dislocation density δ, and lattice constants a and c of the particles obtained according to the XRD spectra. It should be noted that all the results obtained from our samples agree with the values reported in the literature [46,47]. Increasing the deposition times led to an increase in the average crystallite size, which changed from approximately 21 nm to 32 nm for deposition times of 1 min and 9 min, respectively. It is evident that with an increasing spray time of the deposited ZnO films, the intensity of characteristic peaks corresponding to the wurtzite phase gradually increased, indicating an enhancement in both film crystallinity and crystallite size. Similar observations have been reported in the literature for ZnO films [48,49].

The texture coefficient of ZnO crystallites was computed to assess their preferred orientation TC(hkl) [50]

$$TC(hkl) = \left(\frac{I[hkl]_i}{\sum_{n=1}^{n} I[hkl]_i} \right), \qquad (5)$$

where TC hkl is the texture coefficient of the hkl plane. I hkl is the X-ray diffraction intensity of the textured film and n is the number of diffraction peaks considered. The values of the texture coefficients hkl along the (002) plan were calculated. The results of the influence of the disposition time of the preferred orientation are shown in Table III. Increasing deposition times increased the average crystallite size. The size of the crystallites changed from 22-30 nm under deposition time values of 1 and 9 min, respectively. It is clear that, with increasing spray time of the deposited ZnO films the characteristic peaks' intensity of the wurtzite phase is progressively enhanced which reflects the amelioration of both film crystallinity and crystallite size. Similar behavior was reported in the literature for ZnO films [51-54].

In the wurtzite structure of ZnO, according to group theory, the number of atoms per unit cell consists of four atoms. So there are 12 phonon modes *i.e.,* three acoustic phonon modes (one longitudinal-acoustic (LA), two transverse-acoustic (TA)) and nine optical modes (three longitudinal-optical (LO) and six transverse optical (TO) branches) represented by $\Gamma = A_1 + 2B_1 + E_1 + 2E_2$. Where both A_1 and E_1 are Raman and infrared active modes, while B_1 is infrared and silent in Raman scattering modes. A_1 and E_1 symmetries are polar exhibiting two different frequencies for the transverse optical (TO) and longitudinal optical (LO) phonons. While the E_2^{high} modes have two frequencies, E_2^{low} (related to the vibration of the heavy Zn sublattice) and E_2^{high} (related to the vibrations of the oxygen atoms) [55]. Figure 2 shows

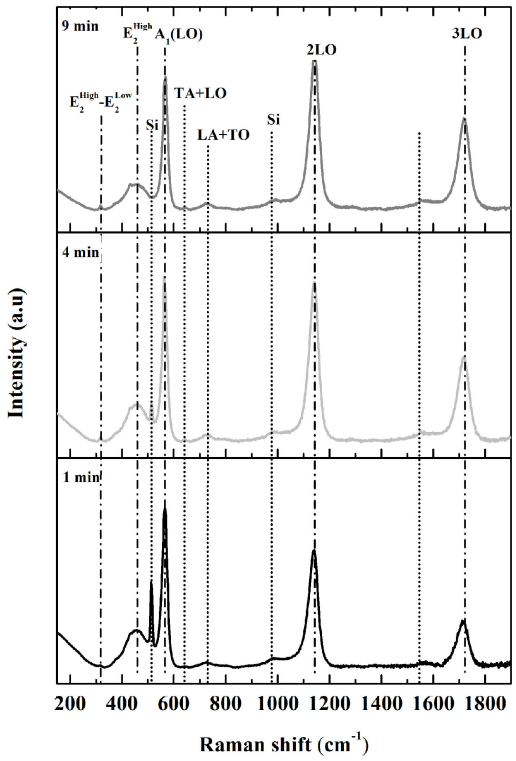

FIGURE 2. Raman spectrum of ZnO thin films with different deposition times (1, 4, and 9 min) deposited on Silicon substrates.

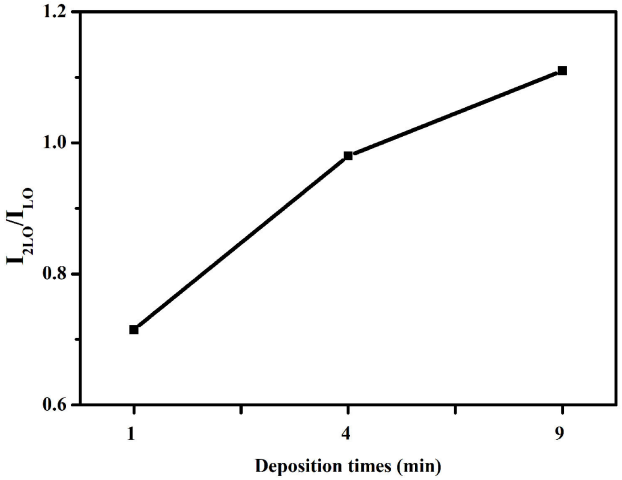

FIGURE 3. Intensity ratio I2LO/ILO of ZnO with different deposition times (1, 4, and 9 min).

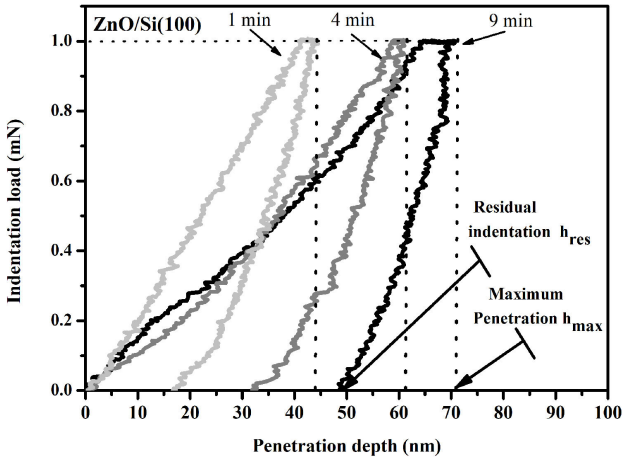

FIGURE 4. The typical load-displacement curves ($p_{\max} = 1$ mN) of the films with different deposition times (1, 4, and 9 min).

the Raman spectrum of ZnO thin films grown at different deposition times (1, 4, and 9 min) in the range of 100-1900 cm^{-1} at room temperature.

The Raman spectra for the applied ZnO films detected seven Raman active modes $E_2^{\text{high}} + A_1(LO) + 2LO + 3LO$, determined by space group analysis TT_{6VV}^4 ($P6_3mc$) [56]. We identify the typical vibration modes for the corresponding ZnO; 323 cm^{-1} for $E_2^{\text{high}} - E_2^{\text{low}}$, 438 cm^{-1} for E_2^{high} (related mostly to the oxygen atoms) [55,57], 520 cm^{-1}, 974 cm^{-1} for Si, 566 cm^{-1} for A1 (LO), 643 cm^{-1} for (TA+LO), 722 cm^{-1} for ($LO + TO$), 1142 cm^{-1} for ($2LO$) and 1720 cm^{-1} for ($3LO$). The results are in good agreement with those of ZnO films in the literature (Table III). The peaks at 520 and 974 cm^{-1} are the Raman mode of substrate [58]. The peak around 438 cm^{-1} is the E_2^{high} mode of wurtzite ZnO, while the peak around 566 corresponds to the A_1 (LO) longitudinal optical mode. The relatively strong intensity of E_2^{high} and A_1 (LO) modes show a ZnO film is highly (002) plane c-axis oriented. This result is consistent with the XRD results shown above. There are two peaks found nearby 1142 and 1720 cm^{-1} are attributed to second-order ($2LO$) and third-order ($3LO$) Raman phonons of ZnO, arising from resonant Raman scattering [59]. It is known that the intensity ratio I_{2LO}/I_{LO} is very sensitive to the electron-phonon coupling strength and that it increases with crystallite size [60]. As shown in Fig. 3, the value has increased with increasing the disposition time where the crystalline size also increases. These results confirm the evolution of estimated crystalline size diffraction data. The observed vibrational modes and their thin film assignments are given in Table IV.

Figure 4 shows the typical load vs. displacement nanoindentation curves for ZnO thin films with different deposition times (1, 4, and 9 min) at a maximum load of 1 mN. Table V shows the matching hardness and elastic modulus values derived from these curves. Notably, the ZnO thin film with a deposition time of 1 min demonstrates the highest hardness and elastic modulus values among all the films. Following this, the ZnO thin film deposited for 4 min exhibits

TABLE IV. Frequencies cm^{-1} and symmetry assignment of Raman vibration mode.

Vibration mode	Peak Assignement	Raman shift (cm^{-1}) in this study for ZnO film	Raman shift (cm^{-1}) in the literature for ZnO film						
			[62]	[63]	[64]	[65]	[45]	[66]	[67]
E_2^{low}	Zn sub lattice	-	98	-	96	-	-	-	97.3
E_2^{High} - E_2^{low}	Multi-phonon process	323	329	333	-	333	-	330	-
A_1 (TO)	Transverse optical mode	-	-	-	-	375	-	379	-
E_1 (TO)	Transverse optical mode	-	-	-	-	410	-	-	-
E_2^{High}	Preferred c-axis orientation	438	436	439	435	443	438	436	437.5
A_1 (LO)	Preferred c-axis orientation	566	537	576	-	563	574	-	-
E_1 (LO)	Formation of defects	-	585	590	-	591	-	566	-
TA + LO	-	643	-	657	-	-	-	-	-
LA + TO	-	722	-	721	-	-	-	-	-
2LO	Second order	1142	1153	1050	-	-	1150	1118	-
3LO	Third order	1720	-	-	-	-	1725	-	-

TABLE V. Hardness, young modulus, depth, and roughness reported in different works.

Mechanical properties	Method	Substrate	Hardness	Young module	Depth	Roughness
References			H (GPa)	Y (GPa)	h (nm)	R (nm)
This study	Ultrasonic spray	304L	9-15	198.7-228.9	43.68-69.61	10-60
304L	-	-	2.12	-	220	43
[68]	Magnetron sputtering R.F	Silicon	4-6	61-125	less than 200	12-12.7
[69]	Magnetron sputtering R.F	Langasite	9.2-10.4	135-160	100-200	13.5-20.6
[70]	Atomic layer deposition (ALD)	Silicon	6.9	143	-	-
[71]	Straightforward mechanoactivated oxidation (MAOM)	Glass	9	120	-	-

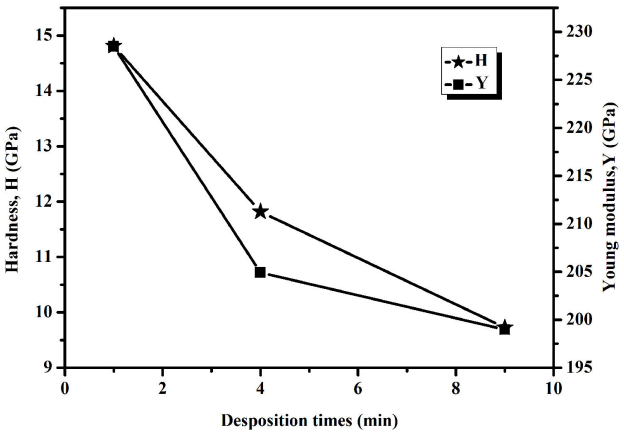

FIGURE 5. Effect of hardness and modulus of elasticity of ZnO with different deposition times (1, 4, and 9 min).

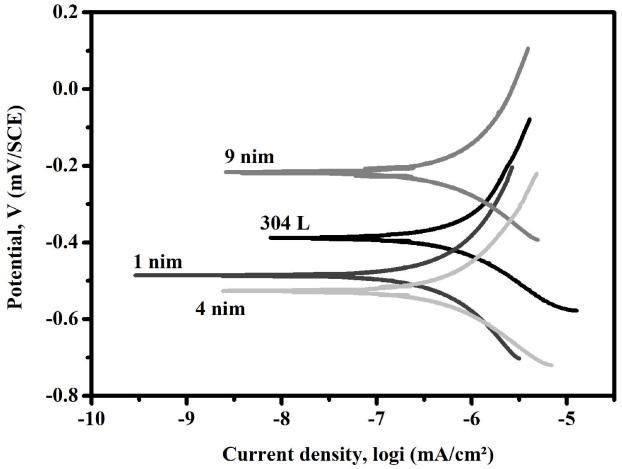

FIGURE 6. Potentiodynamic polarization curves for the ZnO thin films and uncoated 304L stainless steel in Ringer's solution at 37°C with different deposition times (1, 4, and 9 min).

slightly lower values. As expected, the ZnO thin film with a deposition time of 9 min displays the lowest hardness and elastic modulus values.

The effect of ZnO deposition time on the elastic modulus and nano-indentation hardness of the thin film (at a maximum load of 1 mN) is illustrated in Fig. 5. Observing the results, it is evident that there is no significant improvement in hardness with increased ZnO deposition time. Both hardness and Young's modulus decrease as the deposition times are extended. This phenomenon can be attributed to a decrease in grain size [61]. Previous studies, such as those conducted by H. Wang *et al.* [62] and H. M. Wang *et al.* [63], have also performed similar nanoindentation tests on ZnO thin films. Table V gives the hardness and modulus of elasticity values.

Figure 6 shows the potentiodynamic polarization curves of the samples tested in physiological Ringer's solution at 37°C. Two different zones can be seen in the anode and cathode regions of the polarization curve of 304L SS uncoated and coated thin films. For all samples, the cathodic region is the first zone where hydrogen reduction takes place [64]. The second zone, where the current increases, is related to the penetration of the aggressive agent (Cl^-, Na^+, K^+, and Ca^{2+}) into the thin film, and the process is governed by dissolution kinetics. The samples had very low current densities ($Icorr$) than that of 304 L, while the corrosion potential value ($Ecorr$) of the coated sample with time deposition (1 min) is greater when compared to 304 L. The better corrosion resistance shown by the thin film deposited with a time of 9 min suggests the important role of film thickness in increasing corrosion resistance. According to Daubert *et al.* [65], a 50 nm thick ZnO film would enhance the homogeneity of the thin film by decreasing porosity and could provide excellent resistance against corrosion on copper. The experimental results of potentiodynamic polarization indicated an improved corrosion resistance in the ZnO thin films deposited by the ultrasonic spraying method. This is consistent with the results of the inquiry presented by Shajudheen *et al.* [66]. Immersion tests were carried out in the physiological Ringer's solution for 12 h. The authors observed that ZnO thin films significantly improve the corrosion resistance of the 304 L alloy [66]. The Ringer's solution simulating the physiological environment is rich in ions and cations (Cl^-, Na^+, K^+, and Ca^{2+}) components that react with the inner layer of the metallic substrate and cause the pitting of it [67]. According to reports [68], stainless steel is vulnerable to pitting corrosion in aggressive solutions like saline and Ringer's solutions.

TABLE VI. Corrosion parameters for the samples tested in Ringer's solution were determined from the polarization curves.

Parameters	Films	304L	1	4	9
	Units			min	
Corrosion potential (Ecorr)	(mV vs. SCE)	-388	-486	-526	-217
Current density (Icorr)	(μA/cm^2)	2.115	1.354	1.208	0.881
Polarization resistance (Rp)	(KΩ.cm^{-2})	10.518	40.874	61.161	90.358
Corrosion rate (Cr)	(mm/year)	8.97	1.585	1.059	0.715
Cathodic Beta (βc)	(mV)	330.274	490.225	313.31	239.357
Anodic Beta (βa)	(mV)	100.332	652.783	636.887	380.348
Protective efficiency (Pe)	(%)	-	40.68	42.85	58.32
Porosity (P)	(%)	-	0.363	0.241	0.077

The presence of Cl^- on the surface may suggest the creation of an oxide film. Chloride ions in the solution penetrate the porous ZnO film and accelerate the corrosion process of the alloy by forming Cr_2O_3, and Fe_3O_4 [64]. According to the literature, Cl^- ion in Ringer's solution is more than Cl^- ion in NaCl [69]. The results of the polarization curves are in good agreement with the EIS results.

The film protective efficiency (Pe) and the porosity (P) were estimated using the following Eqs. (6) and (7), respectively [43,70,71]:

$$P(\%) = \left(1 - \left[\frac{i_{\text{corr,film}}}{i_{\text{corr,substrates}}}\right]\right), \quad (6)$$

where i_{corr}, film, and i_{corr}, substrates are the corrosion current densities for the thin film and uncoated 304 L electrode, respectively.

$$P = \left(\frac{R_{ps}}{R_p}\right) * 10^{\Delta Ecorr}/b_a, \quad (7)$$

where P is the total porosity of the thin film. R_{ps} is the polarization resistance of the uncoated substrate. R_p is the polarization resistance of the thin film. Δ Ecorr is the difference in the corrosion potential between the coated and uncoated substrate. b_a is the anodic Tafel slope of the substrate. Based on the findings shown in Table VI, we may conclude that the porosity and the protective efficiency values decrease with increasing disposition time. Furthermore, when the disposition time of the ZnO thin film was increased from (1 to 9 min), the Icor value of the ZnO thin film decreased from approximately 1.354 to 0.881 μA/cm^{-2}, indicating that increasing the disposition time would reduce the corrosion resistance. A thin film with a deposited time of 9 min exhibited the best corrosion resistance. These results can be associated with crystal size (Table III).

Table VI presents the corrosion parameters (corrosion potential ($Ecorr$), current density ($Icorr$), Polarization resistance (R_p), Protective efficiency (Pe), Porosity (P), and corrosion rate (CR)) obtained by the Tafel method from the polarization curves in a physiological medium (Ringer's solution at 37°C).

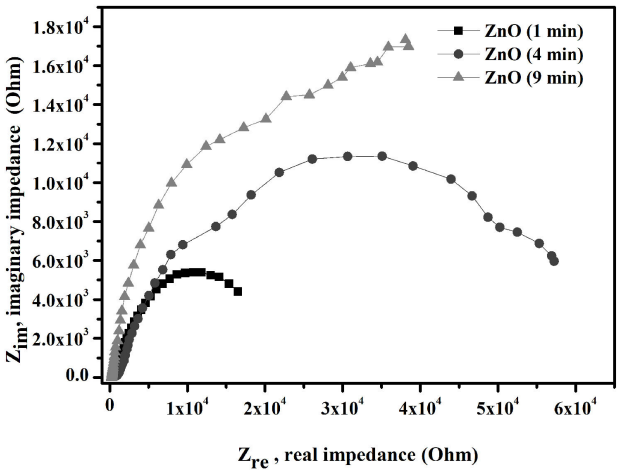

FIGURE 7. Nyquist diagrams of ZnO in Ringer's solution at 37°C with different deposition times (1, 4, and 9 min).

The Nyquist plots for the thin films have been obtained in Ringer's solution after open-circuit measurements over a time (12 h) required to stabilize the EOCP potential (Fig. 7). A single depressed semicircle is shown in the Nyquist diagram for the ZnO/304L electrodes. The diameter of the semicircle of a thin film with a disposition time of 9 min observed from Nyquist plots (Fig. 7) were more significant compared to those deposited within 1 and 4 min, confirming the increase in the corrosion resistance of the thin film with thickness increase. The larger semicircle is caused by the compact thin film and appears at lower frequencies. The semicircle at the low-frequency region for the ZnO curve is associated with the charge transfer resistance at the electrode/electrolyte interface [72]. With the increasing deposition times of ZnO thin films, ions will have difficulty penetrating pores and film defects, which leads to an increase in the charge transfer resistance of ZnO thin films. This increased resistance results in an increase in the diameter of the semi-circle. It indicates the improvement of the corrosion resistance in Ringer's solution. Based on the shapes obtained from the EIS plots, which

TABLE VII. Values of equivalent electric circuits of the ZnO thin coatings in Ringer's physiological solution at 37°C.

ZnO	Corrosion potential (Ecorr) (mV vs.SCE)	Resistance of the electrolyte (Rs) (Ωcm^2)	Constant phase element (CPE) (Ω^{-1}S^{n}cm^{-2})	(n) n	Charge transfer resistance (Rct) (Ωcm^2)
1 min	0.486	75	2.44E-5	0.67	2.02E+3
4 min	0.214	88	1.10E-5	0.68	3.12E+3
9 min	0.527	56	1.60E-6	0.81	6.08E+3

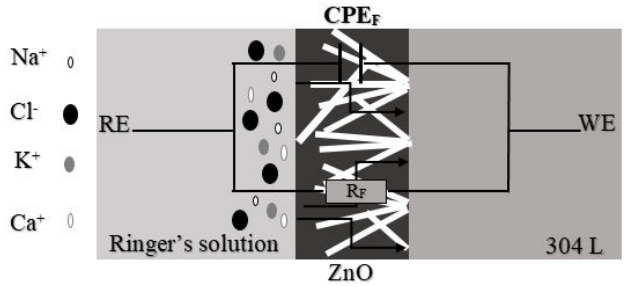

FIGURE 8. Electrical equivalent circuit models of the thin films ZnO/304L in Ringer's solution at 37°C with different deposition times (1, 4, and 9 min).

are characterized by one-time constants, an equivalent electric circuit was chosen to fit the EIS of ZnO films.

In Fig. 8 the equivalent electrical circuit models of the thin films ZnO/304L are presented to explore the corrosion mechanisms of the various samples, the Nyquist data of the ZnO /304L stainless steel thin films with different deposition times were fitted by using the ZView software. As can be seen, the suggested equivalent circuit contains one constant phase element because of one semicircle in their Nyquist plots.

In this circuit, the initial value of the real impedance (Z') corresponds to the solution resistance (Rs), and the diameter of the semicircle of the film is referred to as the charge transfer resistance (Rct) toward diffusion of the electrolyte ions and constant phase element (CPE) is the related capacitive. The derived parameters from the (EIS) for the different deposition times of the ZnO/304L substrate were calculated after fitting the EIS spectra (Table VII). As the deposition time increases, the Rct gradually increases to (6.08×10^3 Ωcm^2). This means that ZnO film prepared at 9 min has the best corrosion resistance.

Figure 9 shows The Mott-Schottky plot of ($1/C^2$) versus the potential for ZnO/304L thin films in a Ringer physiological solution at 37°C. The Mott-Schottky diagram is made for knowing whether the semiconductor is n-type or p-type. The flat-band potential (U_{FB}) of ZnO/304L with different deposition times (1, 4, and 9 min), was performed from the intersection of the straight line to the potential axis (1.69 V, 1.79 V, and 1.99 V), respectively. The analysis showed that all curves give straight lines having a positive slope, which

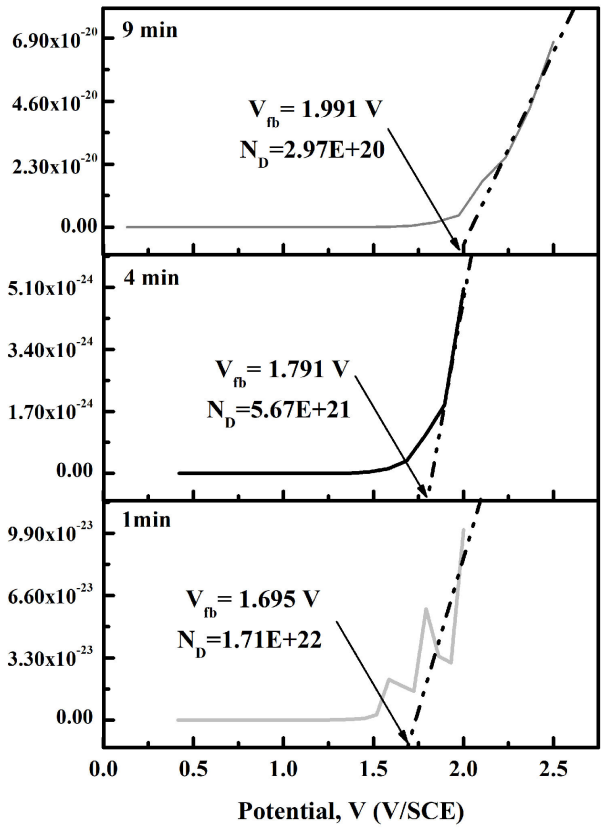

FIGURE 9. The Mott-Schottky plots of $1/C^{-2}$ vs electrode potential for a ZnO formed on 304L with different deposition times (1, 4, and 9 min) in Ringer's solution at 37°C.

indicates that the thin films exhibit an n-type semiconductor. Several authors have confirmed that the ZnO is an n-type semiconductor [6,73,74]. According to the Mott-Schottky theory, Eq. (8) gives the space charge capacitance of an n-type semiconductor.

$$1/C^2 = \left(\frac{2}{\epsilon\epsilon^0 e N_D A^2}\right)\left(U - U_{FB} - \frac{Kb_T}{e}\right). \quad (8)$$

where C is the interfacial capacitance, N_D is the donor density (cm^{-3}), which can be obtained from the slope of the Mott-Schottky plot. U is the applied voltage, U_{FB} the flat-band potential, Kb is Boltzmann's constant, T is the absolute temperature, e is the electronic charge (1.6×10^{-19} C). (A) represents the electrode surface area (0.5 cm^2),

TABLE VIII. Acceptor concentrations (N_D) of the ZnO thin coatings obtained from the linear section of the Mott-Schottky plots given in Fig. 8.

Thin films	Method	Thikness (nm)	Times (min)	Donor N_D(cm^{-3})	Ref.
ZnO/304L	Ultrasonic spray	103	1	1.71E+22	This work
		196	4	5.67E+21	
		278	9	2.97E+20	
ZnO	Sol-gel	-	-	5.4E+18	[57]
ZnO	Sol-gel spin coating	65	-	1.49E+20	[72]
ZnO wires	Electrochemical anodization	50-250	-	1.25E+20	[60]
ZnO Graphite	Thermal chemical vapor deposition	-	-	6.35E+16	[73]

ϵ^0 represents the vacuum permittivity (8.85×10^{-14} F/cm) and ϵ_{Zn} is the passive film's dielectric constant, habitually supposed to be (10 [75]).

The slope of the Mott-Schottky plot gives the donor density (Table VIII), N_D, and the value estimated was (1.71×10^{22} cm^{-3}) for ZnO (1 min) being the highest and for ZnO (9 min) with (2.97×10^{22} cm^3) being the lowest. This slight difference in donor density comes from surface defects and oxygen vacancies in ZnO thin films, which may be associated with a reduction in the electron transport along the oxide [76]. These results are in agreement with those obtained in the EIS analysis. According to Mott-Schottky's theory, the n-type property of a passive film is produced by interstitial diffusion of cations or by anionic diffusion (like oxygen vacancy) in the metal. The density of donors and the slope have an inverse relationship. It suggests that the increase in N_D in a passive film is directly connected with increases in current density values [77]. The higher the donor density, the more susceptible a passive film is to pitting corrosion [77]. In photocatalytic activity, a high donor density value implies a higher carrier concentration, which is related to better conductivity in the films. A high donor density value is normally associated with higher conductivities, enhancing electron effectiveness and hole transport at the electrode interface [76].

4. Conclusion

In this study, we prepared ZnO films on 304L stainless steel by the spray ultrasonic deposition. The structural behavior, Indentation nano measurements, and corrosion behavior (potentiodynamic polarization, electrochemical impedance, and Mott-Schottky analysis) analysis of ZnO films was evaluated, and the following conclusions were drawn.

- ZnO film, formed for various time dispositions, is of polycrystalline structure, with a preferential growth direction along the c-axis. - With the variation of deposition time ranging from 1 to 9 minutes, Young's modulus of the films varied from 198.7 to 228.9 GPa and the hardness varied from 9 to 15 GPa. - The results from nanoindentation affirmed that the time of sputtering deposition significantly influenced the nanomechanical properties of the ZnO film and that the film deposited at 1 minute seemed to have the best mechanical properties.

- The film performed on 304L for 9 min had the highest corrosion resistance: The corrosion protection efficiency of the film was 59 % after 24 h of immersion in Ringer solution. ZnO films have been demonstrated as an effective approach to fabricating corrosion-protective ZnO on 304L alloy.

- Mott-Schottky analysis indicated that thin films formed on 304L displayed an n-type semiconducting behavior. Likewise, this analysis suggested that the donor density is in the range of 10^{22} cm^{-3} and increased with a decrease in the thickness film.

Acknowledgments

We gratefully thank the technical support of S. Sali, and L. Zougar from the Semiconductor Technology Research Center for Energy (CRTSE) Algeria, for their contribution to the completion of this work.

Conflict of interest statement

The authors declare that they have NO affiliations with or involvement in any organization or entity with any financial interest in the subject matter or materials discussed in this manuscript.

1. F. L. Nie, S. G. Wang, Y. Wang, S. C. Wei, Y. F. Zheng, Comparative study on corrosion resistance and in vitro biocompatibility of bulk nanocrystalline and microcrystalline biomedical 304 stainless steel, *Dental Materials*, **27** (2011) 677, https://doi.org/10.1016/j.dental.2011.03.009.
2. D. Xu *et al.*, Accelerated corrosion of 2205 duplex stainless steel caused by marine aerobic Pseudomonas aeruginosa biofilm, *Bioelectrochemistry*, **113** (2017) 1, https://doi.org/10.1016/j.bioelechem.2016.08.001.
3. J. Park, J. S. Kim, D. Y. Lee, and S. H. Lee, Real-time monitoring of stress corrosion cracking in 304 L stainless steel pipe using acoustic emission, *Journal of Nuclear Materials*, **571** (2022) 154009, https://doi.org/10.1016/j.jnucmat.2022.154009.
4. J. R. Aggas, A. Bhat, B. K. Walther, and A. Guiseppi-Elie, Nano-Pt ennobling of stainless steel for biomedical applications, *Electrochimica Acta*, **301** (2019) 153, https://doi.org/10.1016/j.electacta.2019.01.177.
5. P. Bansal, G. Singh, and H. S. Sidhu, Investigation of surface properties and corrosion behavior of plasma sprayed HA/ZnO coatings prepared on AZ31 Mg alloy, *Surface and Coatings Technology*, **401** (2020) 126241, https://doi.org/10.1016/j.surfcoat.2020.126241.
6. S. F. Almojil *et al.*, Constructing a ZnO/CuCo2O4 p-n heterojunction photocatalyst for efficiently hexavalent chromium-phenol detoxification and nitrogen fixation, *Journal of Physics and Chemistry of Solids*, **172** (2023) 111057, https://doi.org/10.1016/j.jpcs.2022.111057.
7. S. Ferraris, and S. Spriano, Antibacterial titanium surfaces for medical implants, *Materials Science and Engineering: C*, **61** (2016) 965, https://doi.org/10.1016/j.msec.2015.12.062.
8. K. Leśniak-Ziółkowska *et al.*, Electrochemical modification of the Ti15Mo alloy surface in solutions containing ZnO and Zn3(PO4)2 particles, *Materials Science and Engineering: C*, **115** (2020) 111098, https://doi.org/10.1016/j.msec.2020.111098.
9. G. Calabrese *et al.*, Structural and antibacterial studies of novel ZnO and ZnxMn1-xO nanostructured titanium scaffolds for biomedical applications, *Biomaterials Advances*, (2022) 213193, https://doi.org/10.1016/j.bioadv.2022.213193.
10. A. Nigam, S. Saini, A. K. Rai, and S. J. Pawar, Structural, morphological, antimicrobial, and cytotoxicity study of spindle-shaped ZnO submicron particles for potential biomedical applications, *Materials Today Communications*, **28** (2021) 102683, https://doi.org/10.1016/j.mtcomm.2021.102683Getrightsandcontent.
11. N. Al-Hardan, M. Abdullah, and A. Abdul Aziz, Effect of low H2 concentrations on the currentvoltage characteristic of ZnO gas sensor, *Advances in Applied Ceramics*, **109** (2010) 436, https://doi.org/10.1179/174367510X12722693956275.
12. S. Mun, M. Maniruzzaman, H.-U. Ko, A. Kafy, and J. Kim, Preparation and characterisation of cellulose ZnO hybrid film by blending method and its glucose biosensor application, *Materials Technology*, **30** (2015) B150, https://doi.org/10.1179/1753555714Y.0000000197.
13. A. Nigam, S. Saini, A.K. Rai, and S.J. Pawar, Structural, optical, cytotoxicity, and antimicrobial properties of MgO, ZnO and MgO/ZnO nanocomposite for biomedical applications, *Ceramics International*, **47** (2021) 19515, https://doi.org/10.1016/j.ceramint.2021.03.289.
14. F. Ahmad, and A. Maqsood, Complex impedance, dielectric constant, electric modulus, and conductivity analysis of Cd doped ZnO nanostructures at high temperatures, *Physica E: Lowdimensional Systems and Nanostructures*, **143** (2022) 115353, https://doi.org/10.1016/j.physe.2022.115353.
15. P.-J. Lu, S.-C. Huang, Y.-P. Chen, L.-C. Chiueh, D.Y.-C. Shih, Analysis of titanium dioxide and zinc oxide nanoparticles in cosmetics, *Journal of Food and Drug Analysis*, **23** (2015) 587, https://doi.org/10.1016/j.jfda.2015.02.009.
16. A. Nigam, S. Pawar, Structural, optical, antimicrobial properties with drug loading and drug release of five different ZnO nano and sub-micron particles for biomedical applications, *Materials Technology*, **37** (2022) 1716, https://doi.org/10.1080/10667857.2021.1978636.
17. I. Erol, Ö. Hazman, M. Aksu, E. Bulut, Synergistic effect of ZnO nanoparticles and hesperidin on the antibacterial properties of chitosan, *Journal of Biomaterials Science, Polymer Edition*, **33** (2022) 1973, https://doi.org/10.1080/09205063.2022.2099668.
18. C.F. Mah, F.K. Yam, Z. Hassan, Investigation and Characterization of ZnO Nanostructures Synthesized by Electrochemical Deposition, *Procedia Chemistry*, **19** (2016) 83, https://doi.org/10.1016/j.proche.2016.03.119.
19. J. Chen, et al., Multi-technique investigation of Ni-doped ZnO thin films on sapphire by metalorganic chemical vapor deposition, *Journal of Vacuum Science & Technology A*, **39** (2021). https://doi.org/10.1116/6.0000816.
20. P. Dutheil, J.C. Orlianges, A. Crunteanu, A. Catherinot, C. Champeaux, AlN, ZnO thin films and AlN/ZnO or ZnO/AlN multilayer structures deposited by PLD for surface acoustic wave applications, *physica status solidi (a)*, **212** (2015) 817, https://doi.org/10.1002/pssa.201431747.
21. R. Schifano *et al.*, Schottky contacts to ZnO layers grown by Atomic Layer Deposition: effects of H2O2 functionalization and transport mechanisms, *Applied Surface Science*, **552** (2021) 149067, https://doi.org/10.1016/j.apsusc.2021.149067.
22. M. Kolhep, C. Sun, J. Bläsing, B. Christian, M. Zacharias, Epitaxial growth of highly textured ZnO thin films on Si using an AlN buffer layer by atomic layer deposition, *Journal of Vacuum Science et Technology A*, **39** (2021) 000793. https://doi.org/10.1116/6.0000793.
23. N. Saoula, L. Bait, S. Sali, M. Azibi, A. Hammouche, and N. Madaoui, Reactive Magnetron Sputter Deposition of Titanium Oxynitride TiNxOy Coatings: Influence of Substrate Bias Voltage on the Structure, *Composition, and Properties, Protection of Metals and Physical Chemistry of Surfaces*, **55** (2019) 743, https://doi.org/10.1134/S207020511904018X.

24. M. Adar *et al*., Elaboration and characterization of zno thin films structural and optical study, *Physics: Conference Series*, **1292** (2019) 012009, https://doi.org/10.1088/1742-6596/1292/1/012009.

25. T. Ramkumar, M. Selvakumar, M. Mohanraj, P. Chandramohan, P. Narayanasamy, Microstructure and corrosion behavior of ZnO-Mg coating on AISI 4140 steel fabricated by spray coating, *Journal of Materials Engineering and Performance*, **29** (2020) 5796, https://doi.org/10.1007/s11665-020-05099-9.

26. Y. Ma *et al*., Improved corrosion protective performance of chitosan coatings reinforced with nano-ZnO on degradable magnesium alloy in simulated body fluid, *Applied Physics A*, **127** (2021) 1, https://doi.org/10.1007/s00339-021-05120-5.

27. M.V. Lungu *et al*., Functional properties improvement of Ag-ZnO thin films using Inconel 600 interlayer produced by electron beam evaporation technique, *Thin Solid Films*, **667** (2018) 76, https://doi.org/10.1016/j.tsf.2018.09.055.

28. Y.D.S. Pambudi *et al.*, Effects of annealing temperature on the electrochemical characteristics of ZnO microrods as anode materials of lithiumion battery using chemical bath deposition, *Ionics*, **25** (2019) 457, https://doi.org/10.1007/s11581-018-2723-z.

29. S. Demirel, N. Savcak, Corrosion Behavior of 304 L Steel Coated with PVB/PAn-Nano Metal Oxide (TiO2, ZnO), *Protection of Metals and Physical Chemistry of Surfaces*, **58** (2022) 592, https://doi.org/10.1134/s2070205122030054.

30. M. Roknian, A. Fattah-alhosseini, S.O. Gashti, and M.K. Keshavarz, Study of the effect of ZnO nanoparticles addition to PEO coatings on pure titanium substrate: Microstructural analysis, antibacterial effect and corrosion behavior of coatings in Ringer's physiological solution, *Journal of Alloys and Compounds*, **740** (2018) 330, https://doi.org/10.1016/J.JALLCOM.2017.12.366.

31. J. Qu, M. Ascencio, L. Jiang, S. Omanovic, and L. Yang, Improvement in corrosion resistance of WE43 magnesium alloy by the electrophoretic formation of a ZnO surface coating, *Journal of Coatings Technology and Research*, **16** (2019) 1559, https://doi.org/10.1007/s11998-019-00212-7.

32. R.T. Heintzkill, K.C. Flannagan-Morris, and N. Abu-Zahra, Surface wetting of silver-doped sol-gel ZnO films, *Surface Engineering*, **36** (2020) 607, https://doi.org/10.1080/02670844.2019.1661144.

33. S. Benramache, Y. Aoun, A. Charef, B. Benhaoua, S. Lakel, Transition width effect on optical characterizations of ZnO thin films deposited by spray ultrasonic, *Inorganic and Nano-Metal Chemistry*, **49** (2019) 177, https://doi.org/10.1080/24701556.2019.1624568.

34. M. Othmane *et al*., Modulation of Physical Properties of Sprayed ZnO Thin Films by Substrate Temperature for Optical Applications, *International Journal of Nanoscience*, **15** (2016) 1650007, https://doi.org/10.1142/S0219581X16500071.

35. C.C.F. Xavier, J.O. Braga, M.O. Pessoa, T. Matencio, and V.F.C. Lins, Corrosion resistance of stainlesssteel surgical tools in enzymatic and alkaline detergent, *Materials Today Communications*, **33** (2022) 104453, https://doi.org/10.1016/j.mtcomm.2022.104453.

36. J. Wu *et al*., Micro mechanical property investigations of Ni-based high-temperature alloy GH4169 based on nanoindentation and CPFE simulation, *International Journal of Solids and Structures*, **258** (2022) 111999, https://doi.org/10.1016/j.ijsolstr.2022.111999.

37. A. Kehal, N. Saoula, S.-E.-H. Abaidia, C. Nouveau, Effect of Ar/N2 flow ratio on the microstructure and mechanical properties of Ti-Cr-N coatings deposited by DC magnetron sputtering on AISI D2 tool steels, *Surface and Coatings Technology*, **421** (2021) 127444, https://doi.org/10.1016/j.surfcoat.2021.127444.

38. A. Burleigh *et al*., Artificial intelligence based analysis of nanoindentation load-displacement data using a genetic algorithm, *Applied Surface Science*, **612** (2023) 155734, https://doi.org/10.1016/j.apsusc.2022.155734.

39. C.C. J. Wang, M. Jin, Y. Zhu, and N. Zhang, The carbon dots modified ZnO films photodetector with broadband and fast photoresponse, *Optical Materials*, **135** (2023) 113341, https://doi.org/10.1016/j.optmat.2022.113341.

40. L. Radjehi, A. Djelloul, S. Lamri, M. F. Slim, and M. Rahim, Oxygen effect on structural and optical properties of zinc oxide, *Surface Engineering*, **35** (2019) 520, https://doi.org/10.1080/02670844.2018.1515842.

41. G. Williamson, and W. Hall, X-ray line broadening from filed aluminium and wolfram, *Acta Metallurgica*, **1** (1953) 22, https://doi.org/10.1016/0001-6160(53)90006-6.

42. M. Dhanam, R. R. Prabhu, and P. Manoj, Investigations on chemical bath deposited cadmium selenide thin films, *Materials Chemistry and Physics*, **107** (2008) 289, https://doi.org/10.1016/j.matchemphys.2007.07.011.

43. N. Madaoui, N. Saoula, L. Zougar, I. Djabrouhou, S. Sali, S. Kermadi, Effect of TiO2 Coating Thickness on the Structure, Mechanical Properties, and Corrosion Behavior of AISI 304L Stainless Steel, *Journal of Materials Engineering and Performance*, (2022) 1, https://doi.org/10.1007/s11665-022-07144-1.

44. M. Xin, Optical properties of nanostructured ZnO:Eu film by sol-gel method, *Surface Engineering*, **35** (2019) 947, https://doi.org/10.1080/02670844.2019.1573344.

45. K. Ravichandran, E. Sindhuja, R. Uma, T. Arun, Photocatalytic efficacy of ZnO films - light intensity and thickness effects, *Surface Engineering*, **33** (2017) 512, https://doi.org/10.1080/02670844.2016.1270797.

46. M. Podia, and A.K. Tripathi, Structural, optical and luminescence properties of ZnO thin films: Role of hot electrons defining the luminescence mechanisms, *Journal of Luminescence*, **252** (2022) 119331, https://doi.org/10.1016/j.jlumin.2022.119331.

47. Z. Khan, A.S. Alshammari, M. Bouzidi, M. Shkir, and D. Shukla, Improved optoelectronic performance of sol-gel derived ZnO nanostructured thin films, *Inorganic Chemistry Communications*, **132** (2021) 108812, https://doi.org/10.1016/j.inoche.2021.108812.

48. Y. Rati *et al.*, Visible light assisted degradation of Rhodamin B by reusable S-doped ZnO thin film photocatalyst, *Optical Materials*, **135** (2023) 113370, https://doi.org/10.1016/j.optmat.2022.113370.

49. A. S. Rini, Y. Rati, A. A. Umar, N. A. Abdullah, Investigation of Structural, Morphological and Optical Properties of Sulfur Doped Zinc Oxide Nanorod, *International Journal of Nanoelectronics, Materials*, **13** (2020) 21, https://dspace.unimap.edu.my:80/xmlui/handle/123456789/69808.

50. M. Azibi, N. Saoula, N. Madaoui, H. Aknouche, Effects of Nitrogen Content on the Structural, Mechanical, and Corrosion Properties of ZrN Thin Films Grown on AISI 316L by Radiofrequency Magnetron Sputtering, *Crystal Research and Technology*, **56** (2021) 2100096, https://doi.org/10.1002/crat.202100096.

51. V. Kumar, N. Singh, R. Mehra, A. Kapoor, L. Purohit, H. Swart, Role of film thickness on the properties of ZnO thin films grown by sol-gel method, *Thin Solid Films*, **539** (2013) 161, https://doi.org/10.1016/j.tsf.2013.05.088.

52. M. Islam, M. Hossain, S. Razzak, M. Haque, and D. Saha, Effect of deposition time on nanostructure ZnO thin films synthesized by modified thermal evaporation technique, *Journal of Nanoscience and Nanotechnology*, **16** (2016) 9190, https://doi.org/10.1166/jnn.2016.12901.

53. Z. Khan, A.S. Alshammari, M. Bouzidi, M. Shkir, and D. Shukla, Improved optoelectronic performance of sol-gel derived ZnO nanostructured thin films, *Inorganic Chemistry Communications*, **132** (2021) 108812, https://doi.org/10.1016/j.inoche.2021.108812.

54. Y. Rati *et al.*, Visible light assisted degradation of Rhodamin B by reusable S-doped ZnO thin film photocatalyst, *Optical Materials*, **135** (2023) 113370, https://doi.org/10.1016/j.optmat.2022.113370.

55. A. S. Rini, Y. Rati, A. A. Umar, N. A. Abdullah, Investigation of Structural, Morphological and Optical Properties of Sulfur Doped Zinc Oxide Nanorod, *International Journal of Nanoelectronics, Materials*, **13** (2020) 21, https://dspace.unimap.edu.my:80/xmlui/handle/123456789/69808.

56. M. Azibi, N. Saoula, N. Madaoui, H. Aknouche, Effects of Nitrogen Content on the Structural, Mechanical, and Corrosion Properties of ZrN Thin Films Grown on AISI 316L by Radiofrequency Magnetron Sputtering, *Crystal Research and Technology*, **56** (2021) 2100096, https://doi.org/10.1002/crat.202100096.

57. V. Kumar, N. Singh, R. Mehra, A. Kapoor, L. Purohit, H. Swart, Role of film thickness on the properties of ZnO thin films grown by sol-gel method, *Thin Solid Films*, **539** (2013) 161, https://doi.org/10.1016/j.tsf.2013.05.088.

58. M. Islam, M. Hossain, S. Razzak, M. Haque, and D. Saha, Effect of deposition time on nanostructure ZnO thin films synthesized by modified thermal evaporation technique, *Journal of Nanoscience and Nanotechnology*, **16** (2016) 9190, https://doi.org/10.1166/jnn.2016.12901.

59. N. C. Vega, B. Straube, O. Marin-Ramirez, and D. Comedi, Low temperature chemical vapor deposition as a sustainable method to obtain c-oriented and highly UV luminescent ZnO thin films, *Materials Letters*, **333** (2023) 133684, https://doi.org/10.1016/j.matlet.2022.133684.

60. G. Demircan *et al*., Sol-gel synthesis of Si-ZnO, Ti-ZnO and Si-Ti-ZnO thin films: Impact of Si and Ti content on structural and optical properties, *Materials Today Communications*, **34** (2023) 105234, https://doi.org/10.1016/j.mtcomm.2022.105234.

61. V. Russo, M. Ghidelli, P. Gondoni, C. S. Casari, A. Li Bassi, Multi-wavelength Raman scattering of nanostructured Al-doped zinc oxide, *Journal of Applied Physics*, **115** (2014) 073508, https://doi.org/10.1063/1.4866322.

62. F. Decremps, J. Pellicer-Porres, A. M. Saitta, J.-C. Chervin, A. Polian, High-pressure Raman spectroscopy study of wurtzite ZnO, *Phys. Rev. B*, **65** (2002) 092101, https://doi.org/10.1103/PhysRevB.65.092101.

63. O. Marin, T. Soliz, J.A. Gutierrez, M. Tirado, C. Figueroa, D. Comedi, Structural, optical and vibrational properties of ZnO: M (M= Al3+ and Sr2+) nano and micropowders grown by hydrothermal synthesis, *Journal of Alloys and Compounds*, **789** (2019) 56, https://doi.org/10.1016/j.jallcom.2019.03.115.

64. G. Dovbeshko *et al*., Raman modes and mapping of graphene nanoparticles on Si and photonic crystal substrates, *Optical Materials: X*, **15** (2022) 100163, https://doi.org/10.1016/j.omx.2022.100163.

65. Z. Mao, C. Fu, X. Pan, X. Chen, H. He, W. Wang, Y. Zeng, Z. Ye, Raman-based measurement of carrier concentration in n-type ZnO thin films under resonant conditions, *Physics Letters A*, **384** (2020) 126148, https://doi.org/10.1016/j.physleta.2019.126148.

66. R. Wang, G. Xu, P. Jin, Size dependence of electron-phonon coupling in ZnO nanowires, *Physical Review B*, **69** (2004) 113303, https://doi.org/10.1103/PhysRevB.69.113303.

67. K. Nur *et al*., Mechanical properties of cold sintered ZnO investigated by nanoindentation and micro-pillar testing, *Journal of the European Ceramic Society*, **42** (2022) 512, https://doi.org/10.1016/j.jeurceramsoc.2021.10.011.

68. H. Wang, R. Li, M. Zhou, J. Cedelle, Z. Huang, Q. Wang, Grain boundary sliding mechanism in plastic deformation of nano-grained YAG transparent ceramics: Generalized self-consistent model and nanoindentation experimental validation, *Journal of the European Ceramic Society*, **37** (2017) 2705, https://doi.org/10.1016/j.jeurceramsoc.2017.02.010.

69. H. M. Wang *et al.*, Unique mechanical properties of nano-grained YAG transparent ceramics compared with coarse-grained partners, *Materials Design*, **105** (2016) 9-15. https://doi.org/10.1016/j.matdes.2016.04.094.

70. L. Liu, Y. Meng, C. Dong, Y. Yan, A.A. Volinsky, and L.-N. Wang, Initial formation of corrosion products on pure zinc in simulated body fluid, *Journal of Materials Science Technology*, **34** (2018) 22712282, https://doi.org/10.1016/j.jmst.2018.05.005.

71. J.S. Daubert *et al*., Corrosion protection of copper using Al2O3, TiO2, ZnO, HfO2, and ZrO2 atomic layer deposition, *ACS Applied Materials Interfaces*, **9** (2017) 4192, https://doi.org/10.1021/acsami.6b13571.

72. M. S. VP, S. Kumar, M. Sivakumar, S. R. Mohan, Enhancement of anticorrosion properties of stainless steel 304L using nanostructured ZnO thin films, *AIMS Materials Science*, **5** (2018) 932, https://doi.org/10.3934/matersci.2018.5.932.

73. R. Nowosielski, A. Bajorek, R. Babilas, Corrosion behavior of bioresorbable Ca-Mg-Zn bulk metallic glasses, *Journal of Non-Crystalline Solids*, **447** (2016) 126, https://doi.org/10.1016/j.jnoncrysol.2016.05.037.

74. A. M. Oje, A. A. Ogwu, A. I. Oje, N. Tsendzughul, S. Ur Rahman, A comparative study of the corrosion and ion release behaviour of chromium oxide coatings exposed to saline, Ringer's and Hank's physiological solutions, *Corrosion Science* **167** (2020) 108533. https://doi.org/10.1016/j.corsci.2020.108533.

75. M. Sabzi, S. M. Far, S. M. Dezfuli, Characterization of bioactivity behavior and corrosion responses of hydroxyapatite-ZnO nanostructured coating deposited on NiTi shape memory alloy, *Ceramics International*, **44** (2018) 21395, https://doi.org/10.1016/j.ceramint.2018.08.197.

76. N. Madaoui *et al*., The effect of substrate bias voltage on the electrochemical corrosion behaviors of thin film deposited on stainless steel by r. f magnetron sputtering, *Protection of Metals and Physical Chemistry of Surfaces*, **53** (2017) 527, https://doi.org/10.1134/S2070205117030157.

77. N. Madaoui, L. Bait, K. Kheyar, and N. Saoula, Effect of argon-oxygen mixing gas during magnetron sputtering on TiO2 coatings, Advances in Materials Science and Engineering, 2017, https://doi.org/10.1155/2017/4926543.

78. G. Ortiz Rabell, M. R. Alfaro Cruz, and I. Juárez-Ramírez, Photochemistry of ZnO/GeO2 film for H2 production, *Journal of Photochemistry and Photobiology A: Chemistry*, **433** (2022) 114185, https://doi.org/10.1016/j.jphotochem.2022.114185.

79. L. Su, Z. Guan, Q. Liu, Y. Zhu, Ohmic-Schottky conversion of ZnO/metal contact modulated by a plasma surface treatment method, *Results in Materials*, **15** (2022) 100290, https://doi.org/10.1016/j.rinma.2022.100290.

80. Y. Wang, Z. J. Peng, Q. Wang, X. L. Fu, Tunable electrical resistivity of oxygen-deficient zinc oxide thin films, *Surface Engineering*, **33** (2017) 217, https://doi.org/10.1080/02670844.2016.1212519.

81. P.J. Navarro-Gázquez *et al*., Influence of Zn(NO3)2 concentration during the ZnO electrodeposition on TiO2 nanosponges used in photoelectrochemical applications, *Ceramics International*, **48** (2022) 14460, https://doi.org/10.1016/j.ceramint.2022.01.339.

82. P. Batista-Grau *et al*., Indirect charge transfer of holes via surface states in ZnO nanowires for photoelectrocatalytic applications, *Ceramics International*, **48** (2022) 21856, https://doi.org/10.1016/j.ceramint.2022.04.170.

83. H. Amegroud *et al*., A comprehensive investigation of the electrochemical behavior of nickel-aluminum bronze alloy in alkaline solution: The effect of film formation potential, *Colloids and Surfaces A: Physicochemical and Engineering Aspects*, **614** (2021) 126126, https://doi.org/10.1016/j.colsurfa.2020.126126.